

# Confined and deconfined spinon excitations in the rectangular-lattice quantum antiferromagnet

N. E. Shaik,<sup>1</sup> E. Fogh,<sup>1</sup> B. Dalla Piazza,<sup>1</sup> B. Normand,<sup>1,2</sup> D. A. Ivanov,<sup>3</sup> and H. M. Rønnow<sup>1</sup>

<sup>1</sup>Laboratory for Quantum Magnetism, Institute of Physics,

Ecole Polytechnique Fédérale de Lausanne (EPFL), CH-1015 Lausanne, Switzerland

<sup>2</sup>PSI Center for Scientific Computing, Theory and Data, CH-5232 Villigen-PSI, Switzerland

<sup>3</sup>Institute for Theoretical Physics, ETH Zürich, CH-8093 Zürich, Switzerland

Fractionalization remains one of the most fascinating manifestations of strong interactions in quantum many-body systems. In quantum magnetism, the existence of spinons – collective magnetic excitations that behave as quasiparticles with fractional quantum numbers – is proven in spin chains, but the criteria for their appearance in higher dimensions remain disputed. Motivated by experiments reporting the observation of spinons at high energies in the square-lattice Heisenberg antiferromagnet, we adopt the approach of extrapolating from where spinons are well defined. We study the dynamical properties of a Gutzwiller-projected wave function, the staggered-flux state, on a rectangular spin-1/2 Heisenberg lattice as a function of the spatial coupling ratio,  $\gamma = J_y/J_x$ . By studying the spectrum and the spinon separation distribution we show how, as the system evolves from one-dimensional (1D) towards 2D, the spinons become progressively more confined over most of reciprocal space, but remain deconfined at specific wave vectors.

*Introduction.*—The emergence of quasiparticles with fractional quantum numbers is a fascinating collective phenomenon. Notable examples include quarks confined as hadrons [1], fractionally charged quasiparticles in the quantum Hall effect [2], spin-charge separation of electrons in one-dimensional (1D) systems [3], solitons in polyacetylene-type molecules [4], and spinons in antiferromagnetic (AFM) spin-1/2 Heisenberg chains [5–7]. While the fractionalization of spin excitations in 1D, represented schematically in Figs. 1(a-b), is clearly demonstrable in theoretical models, the existence of true spinons in higher dimensions remains a challenge. Ideal fractionalization, meaning on all energy scales, is present in certain 2D models that have yet to be realized in quantum materials, but in known systems is replaced by conventional behavior as the two  $S = 1/2$  fractions become confined into  $S = 1$  magnons. While the search continues for materials displaying complete deconfinement as a consequence of sufficiently strong quantum fluctuations, for example when frustration effects act to suppress competing magnetic order, a less strict criterion for fractionalization is the observation of spinonic fingerprints at finite energies.

The idea that magnetic correlations in 2D systems can be dominated by the quantum fluctuations clearly manifest in 1D was proposed originally in the context of high-temperature superconductivity (HTS) [8]. The associated concepts, illustrated in Fig. 1(c), provided a starting point for the study of quantum spin liquids [9, 10]. Although the ground state of the quantum ( $S = 1/2$ ) square-lattice Heisenberg AFM relevant to HTS has long-ranged Néel order and sharp magnon bands at low energies, which have been verified quantitatively in a number of materials [11–14], detailed spectroscopic measurements [12, 15–21] have found anomalous, continuum-like scattering at higher energies. Multiple theoretical studies have debated whether these results indicate extensive magnon bound-state formation [22–26] or a possible deconfinement of single magnons into fractional constituents [21, 27–31].

In this Letter we perform a systematic analysis of fractionalization in the excitation spectrum of the  $S = 1/2$  Heisen-

berg model on a rectangular lattice, i.e. with no frustration. To understand if and how the reports of deconfinement at  $(\pi, 0)$  in the 2D limit are connected to complete deconfinement in 1D, we build on prior work establishing the validity of the staggered-flux state as an accurate description of the ground state of the rectangular-lattice model at all values of the spatial coupling ratio,  $J_y/J_x$ . We analyze the excitation spectrum of the staggered-flux state by using a Monte Carlo method to compute the transverse dynamical structure factor and spinon pair separation. Starting from a quantitatively accurate description of the 1D limit, we demonstrate that increasing  $\gamma$  causes a systematic spreading of confinement in reciprocal space, but explicitly not in energy, until in the square lattice the deconfined nature remains only at the  $(\pi, 0)$  points.

We first review the concept of spin fractionalization with the schematic images of Fig. 1. When a single spin is flipped in a 1D Néel state, it can be regarded as two domain walls whose separation costs no further energy [Fig. 1(a)]. If the macroscopic singlet ground state of a Heisenberg spin chain is visualized as a superposition of short-ranged dimer singlets [only nearest-neighbor valence bonds are shown in Fig. 1(b)], a single spin excitation creates a dimer triplet whose two constituent spins are again free to delocalize. These  $S = 1/2$  excitations were established theoretically by the Bethe Ansatz [32] and have been observed in experiment [5–7]. However, extending the domain-wall image to a 2D Néel state [Fig. 1(c)] shows clearly why a spin flip should preserve  $S = 1$  (magnonic) character, with the 1D string of FM bonds creating linear confinement of putative spinons. This has led to the notion that geometrical frustration strong enough to create a disordered (quantum spin-liquid [9]) ground state [Fig. 1(c)] is required to allow fractionalization in 2D.

From all the reports of zone-boundary scattering anomalies in  $S = 1/2$  square-lattice materials [12, 15–21], the system thought to best realize the minimal, nearest-neighbor-only AFM Heisenberg model is copper formate tetradeuterate (CFTD) [12]. Detailed measurements have revealed [19, 21] that the magnon branch of a renormalized spin-wave theory

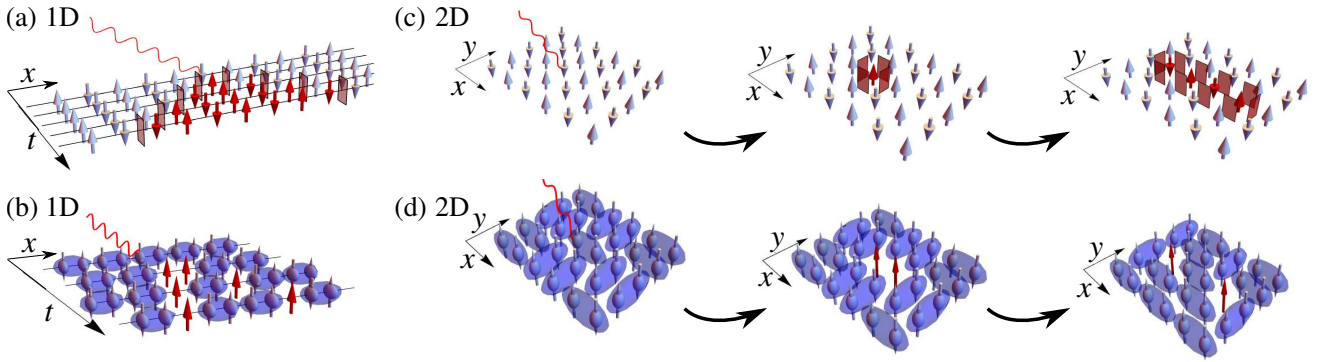


FIG. 1. **Schematic representations of the propagation of spin-flip excitations in low-dimensional quantum spin systems.** (a) A spin flip in a 1D Néel state creates two domain walls, each of which can be interpreted as a spinon. (b) A spin flip in the nearest-neighbor valence-bond state on a chain creates one dimer triplet, whose two uncorrelated spins propagate at no additional energy cost on the singlet background. (c,d) Analogous representations on the AFM square lattice. The propagation of two domain walls in a Néel state creates two lines of ferromagnetic bonds, leading to localization (c). By contrast, in a valence-bond state (d) the two freed spins can still propagate at no extra cost.

survives as a sharp mode everywhere within and on the boundary of the Brillouin zone, except at wave vector  $(\pi, 0)$ , where it loses spectral weight in favor of an apparent scattering continuum at higher energies. The most detailed theoretical and numerical studies of the spectrum, whether based on magnon bound states [25, 26] or on fractionalization [21, 30, 31], have also highlighted the special nature of the  $(\pi, 0)$  points.

*Staggered-flux state on a rectangular lattice.*—It was shown in Ref. [21] that the staggered-flux state [28, 29] on the square lattice exhibits continuum-like scattering and excitations akin to deconfined spinons at the  $(\pi, 0)$  points [33]. To establish whether a spinon interpretation is viable, and if so to connect this putative finite-energy deconfinement in 2D with the complete fractionalization observed in 1D, we therefore adopt the staggered-flux framework. We use it to perform an explicit study of the spectrum of the Heisenberg model on the rectangular lattice (represented in the inset of Fig. 4),

$$\mathcal{H} = \sum_{\mathbf{i}} J_x \mathbf{S}_{\mathbf{i}} \cdot \mathbf{S}_{\mathbf{i}+\hat{x}} + J_y \mathbf{S}_{\mathbf{i}} \cdot \mathbf{S}_{\mathbf{i}+\hat{y}}, \quad (1)$$

by altering the coupling ratio,  $\gamma = J_y/J_x$ , to traverse smoothly from a quasi-1D to a 2D system [34–37].

The staggered-flux state is obtained from the mean-field decoupling of an Ansatz describing the system in terms of fermionic spinons, as we summarize in Sec. S1A of the Supplemental Materials (SM) [38]. The mean-field state,  $|\psi_{\text{SF}}\rangle$ , allows double site occupancy and a Gutzwiller projection,  $|\psi_{\text{GS}}\rangle = P_G |\psi_{\text{SF}}\rangle$ , is performed to obtain the ground state in the physical state space as a variational wave function. In Ref. [39], we optimized the staggered flux in order to discuss the ground state of this rectangular-lattice Heisenberg model [Eq. (1)] as a function of  $\gamma$ . Although the staggered-flux state cannot reproduce the exact ground state of the square-lattice model, most notably lacking an ordered moment, we will show that it offers a valuable starting point for constructing this state in the sense that its finite-energy features, including fractional excitations, provide an excellent account of the

spectral function.

In the variational approach one approximates the physical excitations by projected fermionic excitations [28, 29]. Following Ref. [21], we construct transverse (spin-flip) excitations as linear combinations of fermionic particle-hole pairs,

$$|\psi_{\mathbf{q}}^n\rangle = \sum_{\mathbf{k}} \phi_{\mathbf{k}\mathbf{q}}^n |\mathbf{k}, \mathbf{q}\rangle, \text{ with } |\mathbf{k}, \mathbf{q}\rangle = P_G d_{\mathbf{k}\uparrow}^{\dagger} d_{\mathbf{k}-\mathbf{q}\downarrow}^{-} |\psi_{\text{SF}}\rangle, \quad (2)$$

where  $d_{\mathbf{k}-\mathbf{q}\downarrow}^{-}$  destroys a down spin in the lower band,  $d_{\mathbf{k}\uparrow}^{\dagger}$  creates an up spin in the upper band, and the coefficients  $\phi_{\mathbf{k}\mathbf{q}}^n$  are obtained by diagonalizing the Hamiltonian (1) projected onto the non-orthogonal states  $|\mathbf{k}, \mathbf{q}\rangle$ ; further details are provided in Sec. S1B of the SM [38]. We adopt a Monte Carlo sampling technique to solve the associated generalized eigenvalue problem (Sec. S1C of the SM [38]) and hence to compute the transverse dynamical structure factor (TDSF), which we approximate as

$$S^{\pm}(\mathbf{q}, \omega) = \sum_n |\langle \psi_{\mathbf{q}}^n | S_{\mathbf{q}}^{\pm} | \psi_{\text{GS}} \rangle|^2 \delta(\omega - E_{\mathbf{q}}^n + E_{\text{GS}}), \quad (3)$$

where  $E_{\text{GS}}$  and  $E_{\mathbf{q}}^n$  are respectively the variational energies of the ground and excited states. Thus we perform Monte Carlo simulations on systems of size  $N = L \times L$ , with  $L$  up to 28, working in the space of all singly occupied states with  $N/2+1$  up spins and  $N/2-1$  down spins, and using a statistical average of the energies of the diagonalized Hamiltonian to obtain a suitably  $\mathbf{k}$ -resolved spectrum. Because the staggered-flux wave function is ill-defined at  $\mathbf{k}$ -points  $(\pm\pi/2, \pm\pi/2)$ , we avoid these by keeping antiperiodic boundary conditions (ABCs) in  $y$  while working with both ABCs periodic BCs (PBCs) in  $x$ , which is valuable both for comparison with the exact solution in 1D and for studying finite-size effects in our calculations.

To characterize the spatial profile of these excitations at each  $\mathbf{q}$ , we introduce the weighted spatial spinon density,

$$\rho^q(\mathbf{r}) = \sum_n \frac{|\langle \psi_{\mathbf{q}}^{\dagger}(\mathbf{r}) | \psi_{\mathbf{q}}^n \rangle \langle \psi_{\mathbf{q}}^n | \psi_{\mathbf{q}}(\mathbf{0}) \rangle|^2}{\langle \psi_{\mathbf{q}}^{\dagger}(\mathbf{r}) | \psi_{\mathbf{q}}^{\dagger}(\mathbf{r}) \rangle}, \quad (4)$$

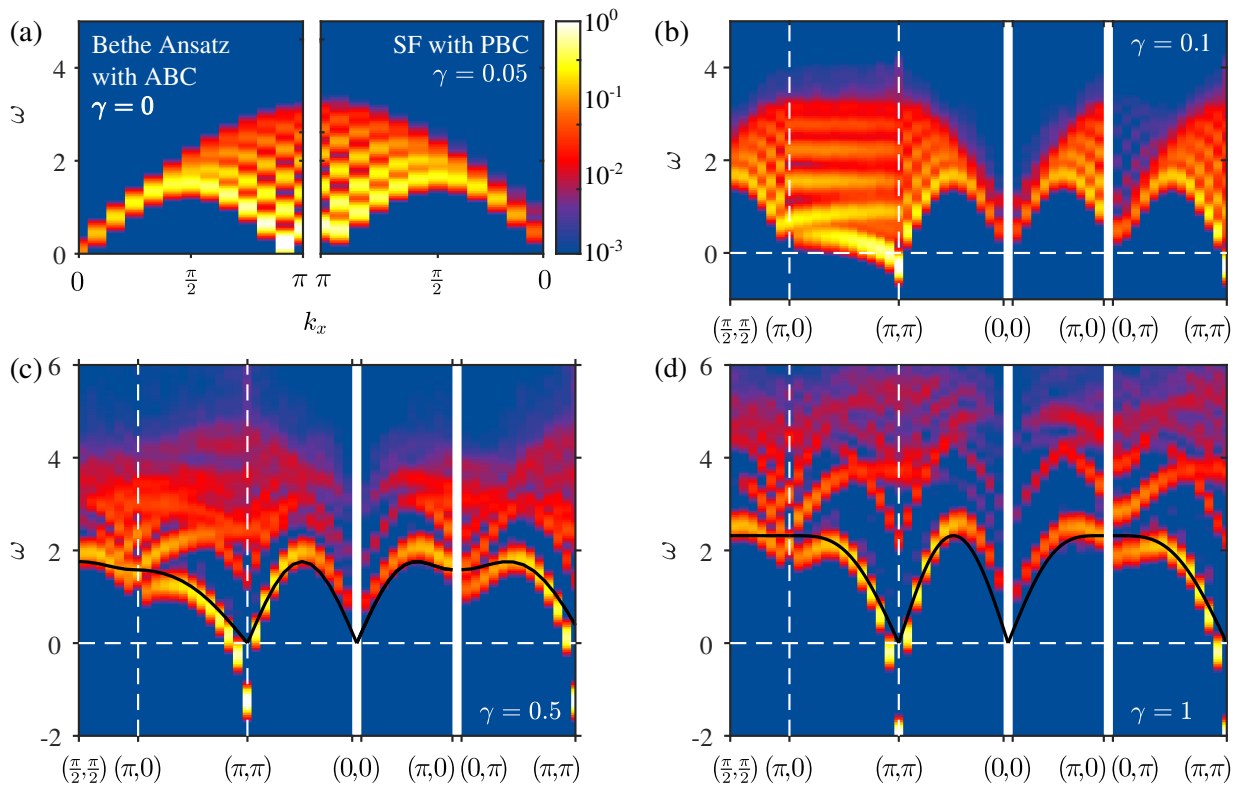


FIG. 2. **Spectral functions on the rectangular lattice.** (a) Comparison between the transverse dynamical structure factors (TDSFs) computed for a chain of  $L = 24$  sites (i.e.  $\gamma = 0$ ) using the algebraic Bethe Ansatz (left) and the staggered-flux state with  $\gamma = 0.05$  (right). (b-d) TDSFs, calculated with PBCs in  $x$  and ABCs in  $y$ , on a selected  $\mathbf{k}$ -path for coupling ratios  $\gamma = 0.1$  (b),  $\gamma = 0.5$  (c), and  $\gamma = 1$  (d) at system size  $L = 24$ . Black lines show the dispersion obtained from the self-consistent spin-wave theory described in Sec. S3 of the SM [38]. The different BCs account for the asymmetry between  $(\pi, 0)$  and  $(0, \pi)$  in panel (d).

where  $|\psi_{\mathbf{q}}^+(\mathbf{r})\rangle$  represents a pair of spinons induced at momentum transfer  $\mathbf{q}$  with a separation  $\mathbf{r} = (x, y)$  (Sec. S1B of the SM [38]). As a means of distinguishing a possible spinon delocalization in 2D from the 1D delocalization we approach in the small- $\gamma$  limit, we define the quantities

$$D_x(\mathbf{q}) = \sqrt{\sum_{\mathbf{r}} x^2 \rho^q(\mathbf{r})} \text{ and } D_y(\mathbf{q}) = \sqrt{\sum_{\mathbf{r}} y^2 \rho^q(\mathbf{r})}. \quad (5)$$

These measure the RMS value of the spinon separation in one lattice direction and hence serve to gauge the degree and nature of spinon deconfinement.

*Results.*—Diagonalizing the projection of  $\mathcal{H}$  onto the  $|\mathbf{k}, \mathbf{q}\rangle$  basis yields  $N$  discrete energies at each value of  $\mathbf{q}$ , which we convolve with Gaussians of width  $\sigma = 0.1J_x$  to obtain the spectra we show in Fig. 2. We begin by benchmarking the validity of the staggered-flux state as a description of the spectrum in the 1D limit, where ideal (fully deconfined) spinons form the basis for the exact solution [32]. Figure 2(a) compares the TDSF calculated using the algebraic Bethe Ansatz [40] with that of a staggered-flux state at  $\gamma = 0.05$  (the lowest coupling we use) and  $q_y = 0$ . We find that the agreement is not only excellent, but quantitatively accurate in energy and intensity when an  $L$ -site chain is compared with an  $L \times L$  rectangular lattice. The  $\gamma = 0.05$  spectrum lies higher in energy

by precisely the finite inter-chain coupling. The fermionic nature of the staggered-flux wave function makes the Bethe Ansatz solution with ABCs equivalent to the staggered-flux state with PBCs and vice versa [39], which is reflected in the  $2\pi/L$  shift in the position of the Goldstone mode near  $k_x = \pi$  in Fig. 2(a). This confirmation lays the foundation for a systematic study of spinon confinement effects when  $\gamma$  is used to bring the system from 1D to 2D.

Figures 2(b-d) show the TDSF for the three coupling ratios  $\gamma = 0.1, 0.5,$  and  $1$  to capture the evolution of the spin dynamics with increasing two-dimensionality. The unphysical negative energies at  $(\pi, \pi)$  reflect how the staggered-flux state, with no long-ranged order, fails to capture the Goldstone mode and the neighboring low-energy spectrum. At all other  $\mathbf{k}$ -points we observe how a quasi-continuum at small coupling ratios [Fig. 2(b)] evolves into sets of discrete modes [Fig. 2(d)]. The loss of spectral weight in the high-energy modes with increasing  $\gamma$  occurs everywhere except at  $(\pi, 0)$ , where these modes continue to provide almost half of the spectral weight at  $\gamma = 1$ . In Sec. S2 of the SM [38] we present a finite-size comparison of different  $\mathbf{k}$ -points in this case. In Figs. 2(c,d) we show also the magnon branch obtained from a self-consistent spin-wave theory [41], which provides an energetic renormalization factor,  $Z_c(\mathbf{k})$ , to linear spin-wave the-

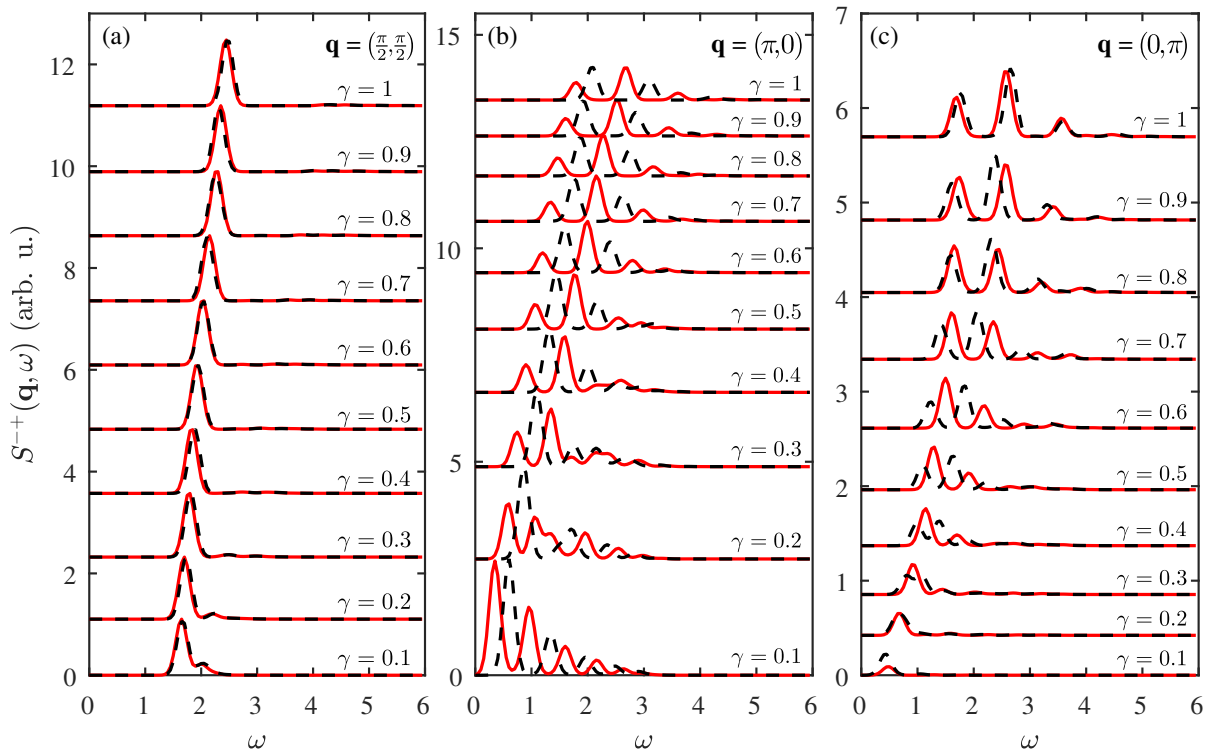


FIG. 3. **Evolution of the TDSF with  $\gamma$ .** TDSF calculated with  $L = 28$  at  $(\pi/2, \pi/2)$  (a),  $(\pi, 0)$  (b), and  $(0, \pi)$  (c). The black lines represent calculations performed with PBCs in  $x$  and ABCs in  $y$ , the red lines ABCs in both directions.

ory as described in Sec. S3 of the SM [38]; away from the negative-energy points we find a rather good match to the low-energy mode of the staggered-flux state.

Figure 3 shows the evolution of the TDSF calculated at  $L = 28$  for the three high-energy points  $(\pi/2, \pi/2)$ ,  $(\pi, 0)$ , and  $(0, \pi)$ . At  $(\pi/2, \pi/2)$  we observe the generic behavior of weak additional modes above the lowest one at low  $\gamma$ , which lose all their weight as the spectrum evolves to contain only a single magnon. At  $(\pi, 0)$ , by contrast, the additional modes retain their weight even at  $\gamma = 1$ , and we show in Sec. S2 of the SM [38] that the real band minimum (the magnon branch) is given by the PBC result in Fig. 3(b), verifying a conjecture made in Ref. [21]. Similar behavior is observed at  $(0, \pi)$  [Fig. 3(c)], although here the spectral weight grows from zero at the 1D limit to fewer, stronger “continuum” modes due to our system size. Extending the insight of Fig. 3 back to Figs. 2(b-d), our results suggest that in the thermodynamic limit the spectrum forms a single, sharp magnon-like mode as  $\gamma \rightarrow 1$ , at all  $\mathbf{k}$ -points other than  $(\pi, 0)$  and  $(0, \pi)$ ; there we find that a series of discrete modes persists, whose number increases with  $L$  (Sec. S2 of the SM [38]), indicating the formation of a 1D-type continuum.

To interpret the line shapes in the TDSF, in Fig. 4 we show the two RMS spinon separations  $D_x(\mathbf{q})$  and  $D_y(\mathbf{q})$  over the high-symmetry directions of  $\mathbf{q}$ -space for the full range of coupling ratios. As  $\gamma$  is increased,  $D_x(\mathbf{q})$  decreases at most  $\mathbf{q}$ -points, reflecting a progressive spinon confinement in the chain direction as a consequence of interchain coupling

[Fig. 4(a)]. By contrast,  $D_x(\mathbf{q})$  provides an excellent illustration of how  $\gamma$  has no effect on confining spinon pairs at wave vectors  $(\pi, 0)$  and  $(0, \pi)$ . Concerning the analogous result at  $(\pi, \pi)$  and  $(0, 0)$ , these low energies are where the staggered-flux state without in-built AF order [21] captures neither the Goldstone mode nor, presumably, the confining effect of the ordered state on the spinons, and hence we do not consider these points further. For further insight into the meaning of deconfinement at  $(0, \pi)$  in this geometry, Fig. 4(b) shows that  $D_y(\mathbf{q})$  is almost invariant with  $\gamma$ , indicating how the trivial spinon localization caused by small interchain coupling turns into a real localization due to the 2D character of the system, with the exception of the growth in RMS separation around the  $(0, \pi)$  and  $(\pi, 0)$  [and  $(\pi, \pi)$  and  $(0, 0)$ ] points.

For a maximally clear visualization of the different behavior of the spinon pair separation, we focus on the points  $(\pi/2, \pi/2)$  and  $(\pi, 0)$  to show the RMS separations as a function of  $\gamma$  in Fig. 5. In the subsidiary panels we show the corresponding spinon pair density distributions at  $\gamma = 0.1, 0.5$ , and 1 on a  $28 \times 28$  lattice. At  $(\pi/2, \pi/2)$ , we observe a gradual decrease of  $D_x(\mathbf{q})$  and a clear localization of the pair density around  $r = 0$  that has almost saturated at  $\gamma = 0.5$ . As with all  $\mathbf{q}$ -points other than the exceptions visible in Fig. 4, this is the characteristic sign of spinon confinement, even though the ground state (the staggered-flux state) has no magnetic order. Again the  $(\pi, 0)$  point is completely different, with  $D_x(\mathbf{q})$  remaining flat and the system-scale 1D distribution turning into a system-scale 2D distribution, indicating that the spinons re-

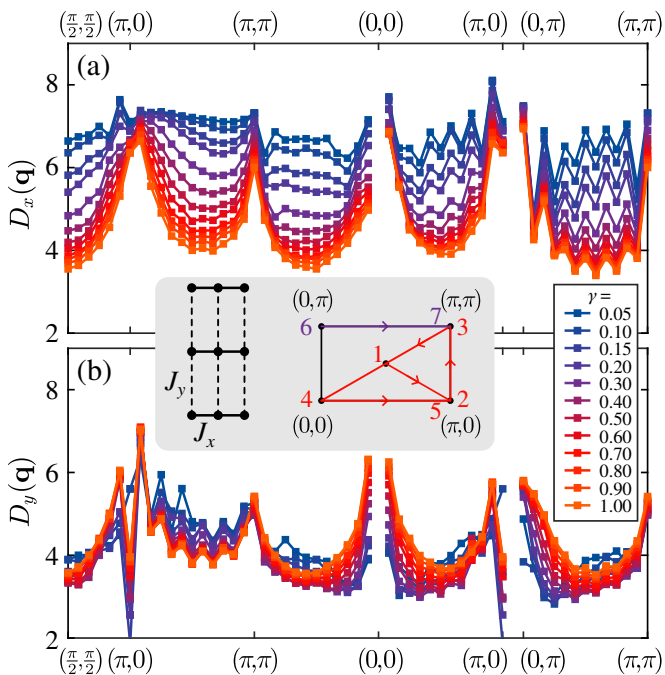


FIG. 4. **RMS spinon pair separation.** Pair-separation parameters  $D_x(\mathbf{q})$  (a) and  $D_y(\mathbf{q})$  (b) calculated on a system of  $L = 24$  with PBCs in  $x$ , shown on the same  $\mathbf{q}$ -space path as in Fig. 2 for different coupling ratios,  $\gamma$ . The inset shows a schematic representation of the rectangular lattice with superexchange couplings  $J_x$  and  $J_y$ , and of the corresponding reciprocal space; numbers 1-7 indicate the order in which the  $\mathbf{q}$ -space path is followed.

main fully deconfined.

*Conclusions.*—We have studied the crossover from 1D to 2D physics in the  $S = 1/2$  Heisenberg model with only nearest-neighbor coupling and no frustration. We base our investigation on a Gutzwiller-projected variational wave function that yields a staggered-flux ground state, and thus we obtain results that are highly indicative but not definitive. By comparison with the Bethe Ansatz solution, we demonstrate that the staggered-flux state provides a quantitatively accurate description of the excitation spectrum in the 1D limit, reproducing the des Cloizeaux-Pearson-Faddeev spinon continuum. Increasing the interchain coupling to the 2D limit causes a systematic vanishing of the spectral weight in all the higher-energy modes at almost all  $\mathbf{q}$ -vectors, leaving only a well-defined magnon mode that can be considered as a pair of confined spinons. Only the reciprocal-space points  $(\pi, 0)$  and  $(0, \pi)$  appear resistant to confinement, with their spectrum retaining a continuum form above its lower edge and their spinon-pair excitations remaining distributed across the entire system.

Our results reinforce the deduction [21] that deconfinement in a 2D system is a reciprocal-space phenomenon, and is not directly connected to the magnon energy. The fact that only two deconfined points survive on the square lattice, taken together with experimental [42] and numerical [43, 44] evidence that deconfinement is more widespread around the zone boundary in the  $S = 1/2$  Heisenberg model on the honey-

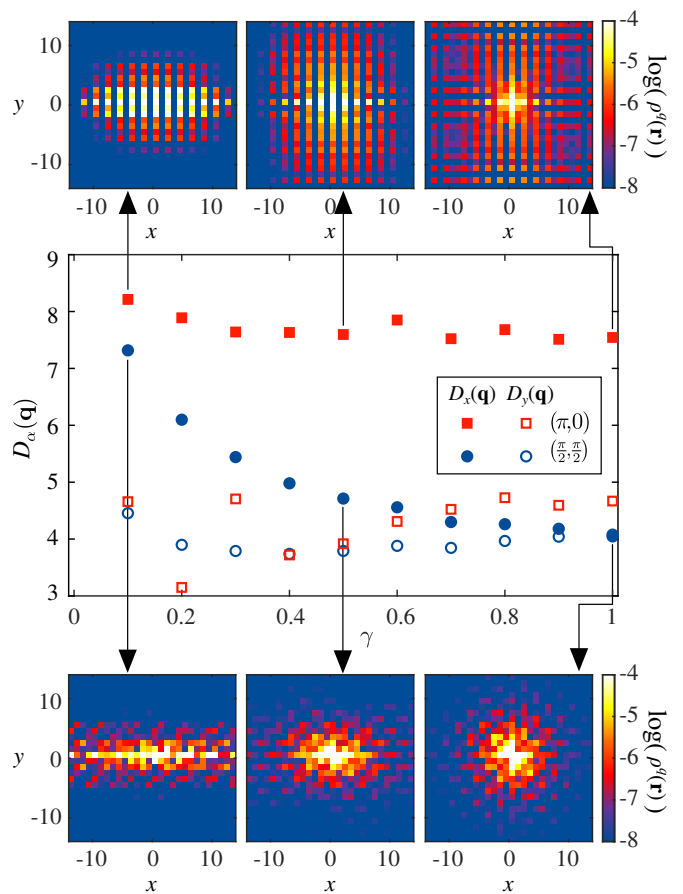


FIG. 5. **Spinon pair separation on the rectangular lattice.**  $D_x(\mathbf{q})$  and  $D_y(\mathbf{q})$  calculated on a system of  $L = 28$  with PBCs in  $x$ , shown as a function of  $\gamma$  at  $\mathbf{q} = (\pi, 0)$  and  $\mathbf{q} = (\pi/2, \pi/2)$ . The subpanels show the corresponding spinon pair-separation distributions,  $\rho^q(\mathbf{r})$ .

comb lattice, indicates that spinon confinement depends sensitively on the kinematics. The confinement transition appears as a smooth crossover, in that the suppression of spinonic behavior at all “conventional”  $\mathbf{k}$ -vectors is a gradual phenomenon, not an abrupt one. Although the  $(\pi, \pi)$  point is a weakness of the staggered-flux wave function, studies of variational states in 2D find long-range order to be a minor modification to a state of otherwise robust quantum fluctuations [45], and hence one expects that such modifications will have little effect on the magnetic excitation spectrum over most of the Brillouin zone. We remark that, because our studies consider finite systems, they do not exclude that spinon confinement occurs in the thermodynamic limit at all finite  $\gamma$  at all wave vectors, other than  $(\pi, 0)$  and  $(0, \pi)$ , but they do show that there is no evidence for a confinement transition at some finite  $\gamma$ . Finally, it is important to remember that both spinons and magnons are quasiparticle approximations to the true many-body excited states, and as such both pictures capture different aspects of these.

*Acknowledgments.*—We thank the European Research Council for financial support through the Synergy network HERO (Grant No. 810451) and the Swiss National Science

Foundation for support through Project Grant No. 188648.

- 
- [1] J. Greensite, *An Introduction to the Confinement Problem*, 1st ed. (Springer, Berlin, Heidelberg, 2011).
- [2] R. B. Laughlin, Anomalous Quantum Hall Effect: An Incompressible Quantum Fluid with Fractionally Charged Excitations, *Phys. Rev. Lett.* **50**, 1395 (1983).
- [3] E. H. Lieb and F. Y. Wu, Absence of Mott Transition in an Exact Solution of the Short-Range, One-Band Model in One Dimension, *Phys. Rev. Lett.* **20**, 1445 (1968).
- [4] W. P. Su, J. R. Schrieffer, and A. J. Heeger, Solitons in Polyacetylene, *Phys. Rev. Lett.* **42**, 1698 (1979).
- [5] D. A. Tennant, R. A. Cowley, S. E. Nagler, and A. M. Tsvelik, Measurement of the spin-excitation continuum in one-dimensional  $\text{KCuF}_3$  using neutron scattering, *Phys. Rev. B* **52**, 13368 (1995).
- [6] B. Lake, D. A. Tennant, C. D. Frost, and S. E. Nagler, Quantum criticality and universal scaling of a quantum antiferromagnet, *Nat. Mater.* **4**, 329 (2005).
- [7] M. Mourigal, M. Enderle, A. Klöpperpieper, J.-S. Caux, A. Stunault, and H. M. Rønnow, Fractional spinon excitations in the quantum Heisenberg antiferromagnetic chain, *Nat. Phys.* **9**, 435 (2013).
- [8] P. W. Anderson, The Resonating Valence Bond State in  $\text{La}_2\text{CuO}_4$  and Superconductivity, *Science* **235**, 1196 (1987).
- [9] L. Savary and L. Balents, Quantum spin liquids: a review, *Rep. Prog. Phys.* **80**, 016502 (2017).
- [10] Y. Zhou, K. Kanoda, and T.-K. Ng, Quantum spin liquid states, *Rev. Mod. Phys.* **89**, 025003 (2017).
- [11] B. Keimer, N. Belk, R. J. Birgeneau, A. Cassanho, C. Y. Chen, M. Greven, M. A. Kastner, A. Aharony, Y. Endoh, R. W. Erwin, and G. Shirane, Magnetic excitations in pure, lightly doped, and weakly metallic  $\text{La}_2\text{CuO}_4$ , *Phys. Rev. B* **46**, 14034 (1992).
- [12] H. M. Rønnow, D. F. McMorrow, R. Coldea, A. Harrison, I. D. Youngson, T. G. Perring, G. Aeppli, O. Syljuåsen, K. Lefmann, and C. Rischel, Spin Dynamics of the 2D Spin- $\frac{1}{2}$  Quantum Antiferromagnet Copper Deuterioformate Tetradeuterate (CFTD), *Phys. Rev. Lett.* **87**, 037202 (2001).
- [13] Y. J. Kim, R. J. Birgeneau, F. C. Chou, M. Greven, M. A. Kastner, Y. S. Lee, B. O. Wells, A. Aharony, O. Entin-Wohlman, I. Y. Korenblit, A. B. Harris, R. W. Erwin, and G. Shirane, Neutron scattering study of  $\text{Sr}_2\text{Cu}_3\text{O}_4\text{Cl}_2$ , *Phys. Rev. B* **64**, 024435 (2001).
- [14] T. Lancaster, S. J. Blundell, M. L. Brooks, P. J. Baker, F. L. Pratt, J. L. Manson, M. M. Conner, F. Xiao, C. P. Landee, F. A. Chaves, S. Soriano, M. A. Novak, T. P. Papageorgiou, A. D. Bianchi, T. Herrmannsdörfer, J. Wosnitzer, and J. A. Schlueter, Magnetic order in the  $S = 1/2$  two-dimensional molecular antiferromagnet copper pyrazine perchlorate  $\text{Cu}(\text{Pz})_2(\text{ClO}_4)_2$ , *Phys. Rev. B* **75**, 094421 (2007).
- [15] R. Coldea, S. M. Hayden, G. Aeppli, T. G. Perring, C. D. Frost, T. E. Mason, S.-W. Cheong, and Z. Fisk, Spin Waves and Electronic Interactions in  $\text{La}_2\text{CuO}_4$ , *Phys. Rev. Lett.* **86**, 5377 (2001).
- [16] M. D. Lumsden, S. E. Nagler, B. C. Sales, D. A. Tennant, D. F. McMorrow, S.-H. Lee, and S. Park, Magnetic excitation spectrum of the square lattice  $S = 1/2$  Heisenberg antiferromagnet  $\text{K}_2\text{V}_3\text{O}_8$ , *Phys. Rev. B* **74**, 214424 (2006).
- [17] N. Tsyrlin, T. Pardini, R. R. P. Singh, F. Xiao, P. Link, A. Schneidewind, A. Hiess, C. P. Landee, M. M. Turnbull, and M. Kenzelmann, Quantum Effects in a Weakly Frustrated  $S = 1/2$  Two-Dimensional Heisenberg Antiferromagnet in an Applied Magnetic Field, *Phys. Rev. Lett.* **102**, 197201 (2010).
- [18] N. S. Headings, S. M. Hayden, R. Coldea, and T. G. Perring, Anomalous High-Energy Spin Excitations in the High- $T_c$  Superconductor-Parent Antiferromagnet  $\text{La}_2\text{CuO}_4$ , *Phys. Rev. Lett.* **105**, 247001 (2010).
- [19] N. B. Christensen, H. M. Rønnow, D. F. McMorrow, A. Harrison, T. G. Perring, M. Enderle, R. Coldea, L. P. Regnault, and G. Aeppli, Quantum dynamics and entanglement of spins on a square lattice, *Proc. Natl. Acad. Sci. U.S.A.* **104**, 15264 (2007).
- [20] K. W. Plumb, A. T. Savici, G. E. Granroth, F. C. Chou, and Y.-J. Kim, High-energy continuum of magnetic excitations in the two-dimensional quantum antiferromagnet  $\text{Sr}_2\text{CuO}_2\text{Cl}_2$ , *Phys. Rev. B* **89**, 180410(R) (2014).
- [21] B. Dalla Piazza, M. Mourigal, N. B. Christensen, G. J. Nilsen, T. Tregenna-Piggott, T. G. Perring, M. Enderle, D. F. McMorrow, D. A. Ivanov, and H. M. Rønnow, Fractional excitations in the square-lattice quantum antiferromagnet, *Nat. Phys.* **11**, 62 (2014).
- [22] R. R. P. Singh and M. P. Gelfand, Spin-Wave Excitation Spectra and Spectral Weights in Square Lattice Antiferromagnets, *Phys. Rev. B* **52**, R15695 (1995).
- [23] A. W. Sandvik and R. R. P. Singh, High-Energy Magnon Dispersion and Multimagnon Continuum in the Two-Dimensional Heisenberg Antiferromagnet, *Phys. Rev. Lett.* **86**, 528 (2001).
- [24] W. Zheng, J. Oitmaa, and C. J. Hamer, Series Studies of the Spin-1/2 Heisenberg Antiferromagnet at  $T = 0$ : Magnon Dispersion and Structure Factors, *Phys. Rev. B* **71**, 184440 (2005).
- [25] M. Powalski, G. S. Uhrig, and K. P. Schmidt, Roton Minimum as a Fingerprint of Magnon-Higgs Scattering in Ordered Quantum Antiferromagnets, *Phys. Rev. Lett.* **115**, 207202 (2015).
- [26] M. Powalski, K. P. Schmidt, and G. S. Uhrig, Mutually attracting spin waves in the square-lattice quantum antiferromagnet, *SciPost Phys.* **4**, 001 (2018).
- [27] A. Auerbach and D. P. Arovas, Spin Dynamics in the Square-Lattice Antiferromagnet, *Phys. Rev. Lett.* **61**, 617 (1988).
- [28] T. C. Hsu, Spin waves in the flux-phase description of the  $S = 1/2$  Heisenberg antiferromagnet, *Phys. Rev. B* **41**, 11379 (1990).
- [29] C.-M. Ho, V. N. Muthukumar, M. Ogata, and P. W. Anderson, Nature of Spin Excitations in Two-Dimensional Mott Insulators: Undoped Cuprates and Other Materials, *Phys. Rev. Lett.* **86**, 1626 (2001).
- [30] H. Shao, Y. Q. Qin, S. Capponi, S. Chesi, Z. Y. Meng, and A. W. Sandvik, Nearly Deconfined Spinon Excitations in the Square-Lattice Spin-1/2 Heisenberg Antiferromagnet, *Phys. Rev. X* **7**, 041072 (2017).
- [31] S.-S. Zhang, E. A. Ghioldi, L. O. Manuel, A. E. Trumper, and C. D. Batista, Schwinger boson theory of ordered magnets, *Phys. Rev. B* **105**, 224404 (2022).
- [32] H. Bethe, Zur Theorie der Metalle, *Z. Phys.* **71**, 205 (1931).
- [33] B. Dalla Piazza, *Theories of Experimentally Observed Excitation Spectra of Square Lattice Antiferromagnets*, Ph.D. thesis, Ecole Polytechnique Fédérale de Lausanne (2014).
- [34] T. Sakai and M. Takahashi, The Ground State of Quasi-One-Dimensional Heisenberg Antiferromagnets, *J. Phys. Soc. Jpn.* **58**, 3131 (1989).
- [35] M. Azzouz, Interchain-coupling effect on the one-dimensional spin-1/2 antiferromagnetic Heisenberg model, *Phys. Rev. B* **48**, 6136 (1993).
- [36] A. Parola, S. Sorella, and Q. F. Zhong, Realization of a spin liquid in a two dimensional quantum antiferromagnet, *Phys. Rev. Lett.* **71**, 4393 (1993).

- [37] T. Miyazaki, D. Yoshioka, and M. Ogata, Anisotropic two-dimensional Heisenberg model studied by the Schwinger-boson Gutzwiller-projection method, *Phys. Rev. B* **51**, 2966 (1995).
- [38] See the Supplemental Materials at <http://www.xxx.yyy>, which contain Refs. [46–48], for a summary of the Gutzwiller-projected variational wave-function approach using the staggered-flux Ansatz to compute spin excitations, for a discussion of the finite-size evolution of the TDSF, and for a review of the self-consistent spin-wave treatment.
- [39] N. E. Shaik, B. Dalla Piazza, D. A. Ivanov, and H. M. Rønnow, Staggered flux state for rectangular-lattice spin- $\frac{1}{2}$  Heisenberg antiferromagnets, *Phys. Rev. B* **102**, 214413 (2020).
- [40] J.-S. Caux, R. Hagemans, and J. M. Maillet, Computation of dynamical correlation functions of Heisenberg chains: the gapless anisotropic regime, *J. Stat. Mech. Theory Exp.* **2005**, P09003 (2005).
- [41] N. E. Shaik, *From quantum spin chains to square lattice Heisenberg antiferromagnets*, Ph.D. thesis, Ecole Polytechnique Fédérale de Lausanne (2019).
- [42] C. Wessler, B. Roessli, K. W. Krämer, B. Delley, O. Waldmann, L. Keller, D. Cheptiakov, H. B. Braun, and M. Kenzelmann, Observation of plaquette fluctuations in the spin-1/2 honeycomb lattice, *npj Quantum Mater.* **5**, 85 (2020).
- [43] C. Gu, S.-L. Yu, and J.-X. Li, Spin dynamics and continuum spectra of the honeycomb  $J_1$ - $J_2$  antiferromagnetic Heisenberg model, *Phys. Rev. B* **105**, 174403 (2022).
- [44] J. A. Hernández, A. A. Eberharter, M. Schuler, J. Lass, D. G. Mazzone, R. Sibille, S. Raymond, K. W. Krämer, B. Normand, B. Roessli, A. M. Läuchli, and M. Kenzelmann, Field-Induced Magnon Decay, Magnon Shadows, and Roton Excitations in the Honeycomb Antiferromagnet YbBr<sub>3</sub> (2024), arXiv:2412.17720.
- [45] S. Liang, B. Doucot, and P. W. Anderson, Some New Variational Resonating-Valence-Bond-Type Wave Functions for the Spin-1/2 Antiferromagnetic Heisenberg Model on a Square Lattice, *Phys. Rev. Lett.* **61**, 365 (1988).
- [46] E. Manousakis, The spin-1/2 Heisenberg antiferromagnet on a square lattice and its application to the cuprous oxides, *Rev. Mod. Phys.* **63**, 1 (1991).
- [47] T. Holstein and H. Primakoff, Field Dependence of the Intrinsic Domain Magnetization of a Ferromagnet, *Phys. Rev.* **58**, 1098 (1940).
- [48] T. Oguchi, Theory of Spin-Wave Interactions in Ferro- and Antiferromagnetism, *Phys. Rev.* **117**, 117 (1960).

## Supplemental Materials to accompany the manuscript

### Confined and deconfined spinon excitations in the rectangular-lattice quantum antiferromagnet

N. E. Shaik, E. Fogh, B. Dalla Piazza, B. Normand, D. Ivanov, and H. M. Rønnow

#### S1. SPIN EXCITATIONS IN THE STAGGERED-FLUX STATE

##### A. Staggered-flux wave function

In order to provide a self-contained presentation, here we summarize the Gutzwiller-projected variational wave-function approach using the staggered-flux Ansatz. The construction of the wave function and optimization of the variational parameters are described in detail in Ref. [39].

The Heisenberg interaction may be expressed in terms of auxiliary (“slave”) fermions as

$$\begin{aligned} \mathcal{H}_{\langle i,j \rangle} &= J_{ij} \mathbf{S}_i \cdot \mathbf{S}_j \\ &= -\frac{1}{2} J_{ij} [n_i (\frac{1}{2} n_j - 1) + \sum_{\alpha\beta} c_{i\alpha}^\dagger c_{j\alpha} c_{j\beta}^\dagger c_{i\beta}], \end{aligned} \quad (\text{S1})$$

where  $i, j$  are pairs of nearest-neighbor sites,  $\alpha$  and  $\beta$  are spin flavors, and  $n_i$  is the fermion number operator at site  $i$ . The first term is constant at half electronic filling and is neglected henceforth. The second term may be treated at the mean-field level by a standard decoupling scheme, and to describe the spin excitations in the absence of magnetic order [21] we con-

sider the staggered-flux fermionic Hamiltonian

$$H_{\text{SF}} = - \sum_{\langle i,j \rangle, \sigma} \chi_{i,j} c_{i\sigma}^\dagger c_{j\sigma} \quad (\text{S2})$$

with the hopping amplitudes

$$\chi_{i,i+x} = \chi_x e^{i(-1)^{i_x+i_y} \varphi/4}, \quad (\text{S3})$$

$$\chi_{i,i+y} = \chi_y e^{-i(-1)^{i_x+i_y} \varphi/4}. \quad (\text{S4})$$

The ground state of  $H_{\text{SF}}$  depends on the two parameters  $\alpha = \chi_x/\chi_y$  and  $\varphi$ , whose systematic dependence on  $\gamma$  was studied in Ref. [39].

Diagonalizing  $H_{\text{SF}}$  (S2) yields the eigenenergies

$$\varepsilon_{\mathbf{k}}^\pm = \pm \frac{1}{2} |\chi_x e^{i\varphi/4} \cos k_x + \chi_y e^{-i\varphi/4} \cos k_y|, \quad (\text{S5})$$

which describe the dispersion relation of spinon excitations that are gapless at point nodes located at  $(\pm\pi/2, \pm\pi/2)$ . The corresponding eigenoperators are  $d_{\mathbf{k}\sigma}^\pm$  and  $d_{\mathbf{k}\sigma}^{\pm\dagger}$ , which are combinations of the  $c$  and  $c^\dagger$  operators that respectively annihilate or create spinons of spin  $\sigma$  in a lower (−) or an upper (+) band in the magnetic Brillouin zone. The ground state of  $H_{\text{SF}}$  may then be expressed as

$$|\psi_{\text{SF}}\rangle = \prod_{\mathbf{k} \in \text{MBZ}} d_{\mathbf{k}\uparrow}^- d_{\mathbf{k}\downarrow}^- |0\rangle, \quad (\text{S6})$$

where  $|0\rangle$  is the fermionic vacuum. This wave function spans an eigenspace that includes sites in real space with double fermion occupation. The physical space of states with exactly one fermion per site is reached by applying a Gutzwiller projector,  $P_G$ , to obtain the ground-state wave function

$$|\psi_{\text{GS}}\rangle = P_G |\psi_{\text{SF}}\rangle. \quad (\text{S7})$$

### B. Spin Excitations

We construct spin excitations from the variational wave function as Gutzwiller-projected pairs of spinons (fermions and holes). Here we summarize the procedure described in Ref. [21]. We refer to spin-flipping excitations ( $\sigma \leftrightarrow \bar{\sigma}$ ) as transverse and to non-spin-flip processes as longitudinal; because we consider the staggered-flux state without building in magnetic order, the transverse ( $S_{\mathbf{q}}^+$ ) and longitudinal ( $S_{\mathbf{q}}^z$ ) components should be equivalent and we focus only on the former. The basis vectors of the excitation subspace are given by applying the Gutzwiller projector to the space of mean-field states with a single particle-hole pair,

$$|\mathbf{k}, \mathbf{q}\rangle = P_G d_{\mathbf{k}\uparrow}^{+\dagger} d_{\mathbf{k}-\mathbf{q}\downarrow}^- |\psi_{\text{SF}}\rangle \quad (\text{S8})$$

where  $\mathbf{q}$  the physical momentum of the spin excitation and  $\mathbf{k}$  is the internal relative momentum of the spinons. The eigenstates in this excitation subspace may then be expressed in the form

$$|\psi_{\mathbf{q}}^n\rangle = \sum_{\mathbf{k}} \phi_{\mathbf{k}\mathbf{q}}^n |\mathbf{k}, \mathbf{q}\rangle, \quad (\text{S9})$$

where  $n$  labels the number of the state in ascending order of energy. Diagonalization of the Hamiltonian [Eq. (1) of the main text] in the non-orthogonal  $|\mathbf{k}, \mathbf{q}\rangle$  basis is performed by solving the generalized eigenvalue problem

$$\sum_{\mathbf{k}'} H_{\mathbf{k}\mathbf{k}'}^q \phi_{\mathbf{k}'\mathbf{q}}^n = E_{\mathbf{q}}^n \sum_{\mathbf{k}'} O_{\mathbf{k}\mathbf{k}'}^q \phi_{\mathbf{k}'\mathbf{q}}^n, \quad (\text{S10})$$

where

$$H_{\mathbf{k}\mathbf{k}'}^q = \langle \mathbf{k}, \mathbf{q} | \mathcal{H} | \mathbf{k}', \mathbf{q} \rangle, \quad O_{\mathbf{k}\mathbf{k}'}^q = \langle \mathbf{k}, \mathbf{q} | \mathbf{k}', \mathbf{q} \rangle, \quad (\text{S11})$$

and we assume the eigenstates of Eq. (S9) to be correctly normalized.

To quantify the real-space structure of the spin excitations, we define the state

$$|\psi_{\mathbf{q}}^+(\mathbf{r})\rangle = P_G \sum_{\mathbf{r}'} e^{i\mathbf{q}\cdot\mathbf{r}'} d_{\mathbf{r}+\mathbf{r}'\uparrow}^{+\dagger} d_{\mathbf{r}'\downarrow}^- |\psi_{\text{SF}}\rangle, \quad (\text{S12})$$

which describes a spin-flip operation for a pair of spinons with propagation vector  $\mathbf{q}$  that are separated by a distance  $\mathbf{r}$ . In the momentum basis, this delocalized spin flip can be expressed as

$$|\psi_{\mathbf{q}}^+(\mathbf{r})\rangle = \sum_{\mathbf{k}} \phi_{\mathbf{k}\mathbf{q}}^+(\mathbf{r}) |\mathbf{k}, \mathbf{q}\rangle, \quad (\text{S13})$$

where the coefficients  $\phi_{\mathbf{k}\mathbf{q}}^+(\mathbf{r})$  can be evaluated from the coefficients of the Bogoliubov transformation defining  $d_{\mathbf{k}\sigma}^{\pm}$  and  $d_{\mathbf{k}\sigma}^{\pm\dagger}$  [21]. The quantity we use in Eq. (4) of the main text to characterize the spinon separation can be understood as a time-averaged density of spinons prepared initially at zero separation: taking

$$\rho^q(\mathbf{r}, t) = \frac{|\langle \psi_{\mathbf{q}}^+(\mathbf{r}) | e^{-i\mathcal{H}t} | \psi_{\mathbf{q}}^+(\mathbf{0}) \rangle|^2}{\langle \psi_{\mathbf{q}}^+(\mathbf{r}) | \psi_{\mathbf{q}}^+(\mathbf{r}) \rangle}, \quad (\text{S14})$$

introducing  $\sum_n |\psi_{\mathbf{q}}^n\rangle \langle \psi_{\mathbf{q}}^n|$  as a resolution of the identity, and integrating the  $e^{-iE_{\mathbf{q}}^n t}$  factors over all time leads to

$$\begin{aligned} \rho^q(\mathbf{r}) &= \lim_{T \rightarrow \infty} \frac{1}{T} \int_0^T \rho^q(\mathbf{r}, t) dt \\ &= \sum_n \frac{|\langle \psi_{\mathbf{q}}^+(\mathbf{r}) | \psi_{\mathbf{q}}^n \rangle \langle \psi_{\mathbf{q}}^n | \psi_{\mathbf{q}}^+(\mathbf{0}) \rangle|^2}{\langle \psi_{\mathbf{q}}^+(\mathbf{r}) | \psi_{\mathbf{q}}^+(\mathbf{r}) \rangle}. \end{aligned} \quad (\text{S15})$$

We note here that our definition [Eq. (S14)] differs slightly from that of Ref. [21], in that we have chosen to normalize the states  $|\psi_{\mathbf{q}}^+(\mathbf{r})\rangle$  to provide a more transparent interpretation of this measure without changing the qualitative results.

### C. Monte Carlo calculations

Following Ref. [21], the Gutzwiller projector in the excitation subspace can be written in the form  $P_G = \sum_{\alpha} |\alpha\rangle \langle \alpha|$ , where  $\{|\alpha\rangle\}$  is the set of states with a single transverse (particle-hole) excitation that is also singly occupied in the site basis, meaning that for a system of  $N = L \times L$  sites it has  $\frac{1}{2}N + 1$  up and  $\frac{1}{2}N - 1$  down spins. Because this space grows exponentially with  $N$ , the Hamiltonian in the particle-hole space can only be computed for a small system, or for a larger finite system by an approximate method, for which we adopt an approach of Monte Carlo sampling. We rearrange the elements of the Hamiltonian in the form

$$\begin{aligned} \frac{H_{\mathbf{k}, \mathbf{k}'}^q}{W_{\mathbf{q}}} &= \sum_{\alpha} \frac{W_{\mathbf{q}}(\alpha)}{W_{\mathbf{q}}} \sum_{\beta} \frac{\langle \mathbf{k}, \mathbf{q} | \alpha \rangle \langle \alpha | \mathcal{H} | \beta \rangle \langle \beta | \mathbf{k}', \mathbf{q} \rangle}{W_{\mathbf{q}}(\alpha)} \\ &\equiv \sum_{\alpha} \rho(\alpha) f(\alpha), \end{aligned}$$

where

$$W_{\mathbf{q}} = \sum_{\alpha} W_{\mathbf{q}}(\alpha) = \sum_{\mathbf{k}\alpha} |\langle \alpha | \mathbf{k}, \mathbf{q} \rangle|^2 \quad (\text{S16})$$

$$= \sum_{\mathbf{k}} \langle \mathbf{k}, \mathbf{q} | \mathbf{k}, \mathbf{q} \rangle = \text{Tr } O^q \quad (\text{S17})$$

expresses the normalization arising due to the non-orthonormal nature of the  $|\mathbf{k}, \mathbf{q}\rangle$  basis. Because the elements of the Hamiltonian matrix appear now as a weighted average over a function, schematically  $f(\alpha)$ , with weights  $\rho(\alpha)$ , they can be estimated from Monte Carlo simulations performed in the space of states  $\{|\alpha\rangle\}$ .



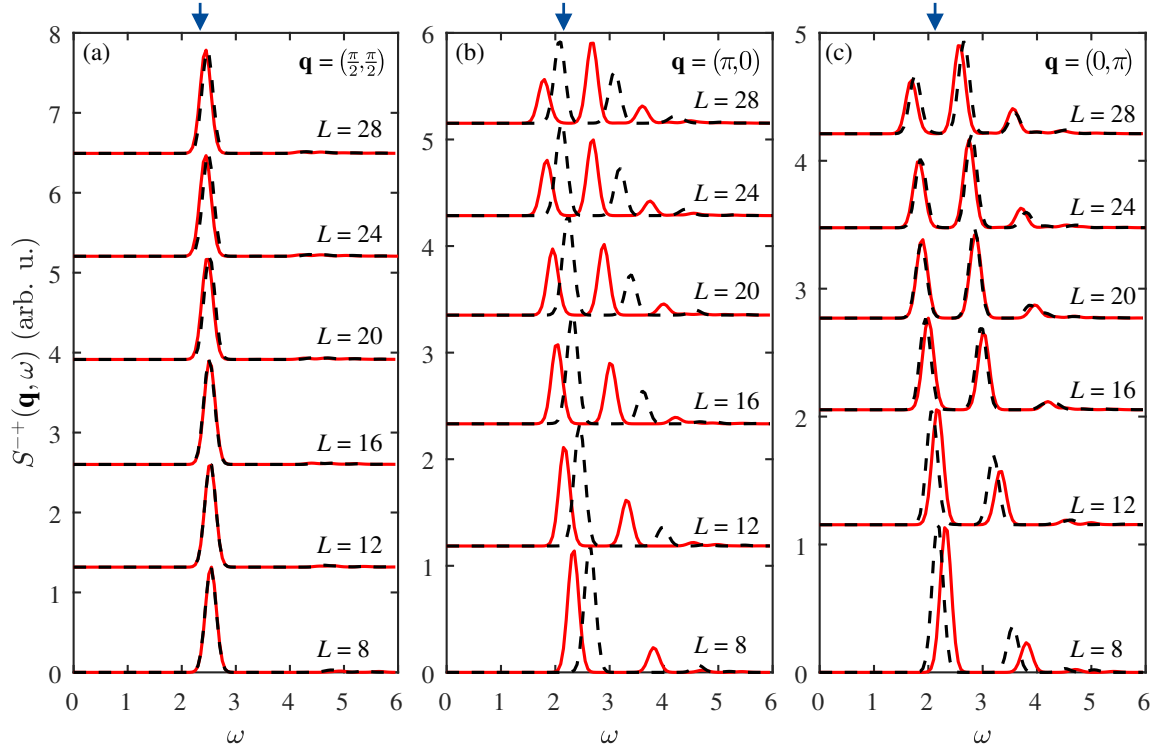


FIG. S1. **Finite-size evolution of the TDSF.** TDSF shown for  $\gamma = 1$  at  $(\pi/2, \pi/2)$  (a),  $(\pi, 0)$  (b), and  $(0, \pi)$  (c) for increasing system sizes,  $L$ . The solid red line shows results computed with ABCs in  $x$  and the dashed black line PBCs. The arrows mark the lowest excitation energies expected from a combination of theoretical [46], numerical [26, 30], and experimental [20, 21] methods, which benchmark the rate of convergence of our results with system size.

In a similar way, we compute the overlap matrix  $O_{\mathbf{k}\mathbf{k}'}^q/W_{\mathbf{q}}$ . The overall normalization of  $H_{\mathbf{k}\mathbf{k}'}^q$  and  $O_{\mathbf{k}\mathbf{k}'}^q$  by  $W_{\mathbf{q}}$  is not relevant for the generalized eigenvalue problem of Eq. (S10), but is important to take into account for the calculation of other quantities. An important example for our purposes is the TDSF, which we calculate as

$$\begin{aligned} S^{\pm}(\mathbf{q}, \omega) &= \sum_n \langle \psi_{\mathbf{G}\mathbf{S}} | S_{\mathbf{q}}^{-} | \psi_{\mathbf{q}}^n \rangle \langle \psi_{\mathbf{q}}^n | S_{\mathbf{q}}^{+} | \psi_{\mathbf{G}\mathbf{S}} \rangle \delta(\omega - \omega_n) \\ &= \sum_n \left| \sum_{\mathbf{k}\mathbf{k}'} \phi_{\mathbf{k}\mathbf{q}}^{n*} O_{\mathbf{k}\mathbf{k}'}^q \phi_{\mathbf{k}'\mathbf{q}}^n \right|^2 \delta(\omega - \omega_n). \end{aligned} \quad (\text{S18})$$

Here the normalization at each  $\mathbf{q}$  is lost because of factors of  $W_{\mathbf{q}}$ , and can be restored by using the sum rule equating the energy-integrated TDSF to the instantaneous transverse spin correlation function [21].

## S2. FINITE-SIZE ANALYSIS OF THE TDSF AT SELECTED HIGH-SYMMETRY POINTS

All of our calculations are performed on square systems ( $L_x = L_y = L$ ) with even  $L$ , maintaining ABCs in the  $y$  direction, while in the  $x$  direction we compare both PBCs and ABCs. For practical purposes, in addition to avoiding the nodal points [ $k = (\pm\pi/2, \pm\pi/2)$ ], the comparison highlights that modes well defined in  $\mathbf{k}$ -space are largely independent

of the BCs, whereas peaks appearing as the finite-size analog of a continuum change their positions significantly when the BCs are changed.

This physics offers direct numerical insight into the continuum or discrete nature of the spectrum as the thermodynamic limit is approached. In Fig. S1 we show the evolution of the TDSF at  $\gamma = 1$  with the system size for both types of  $x$ -axis BCs. Considering first the size effect, increasing  $L$  causes very little change at the magnon-like  $(\pi/2, \pi/2)$  point, whereas at  $(\pi, 0)$  and  $(0, \pi)$  we find an increasing number of equally spaced modes, suggesting a continuum as  $L \rightarrow \infty$ . The loss of spectral weight in the lowest-energy mode at  $(\pi, 0)$  with ABCs [Fig. S1(b)], and the gain in the second mode, confirms the statement made in the main text about the correct identification of the magnon branch (which is the lower bound of the emerging continuum).

Turning to the effect of the BCs, this is clearest at large  $L$ , where the single peak at  $(\pi/2, \pi/2)$  is barely affected [Fig. S1(a)], whereas the multiple peaks at  $(\pi, 0)$  shift by approximately half of their energetic spacing [Fig. S1(b)]. At  $(0, \pi)$  the peak positions are little affected by the  $x$ -axis BCs [Fig. S1(c)], but would change with the  $y$ -axis BCs as in Fig. S1(b).

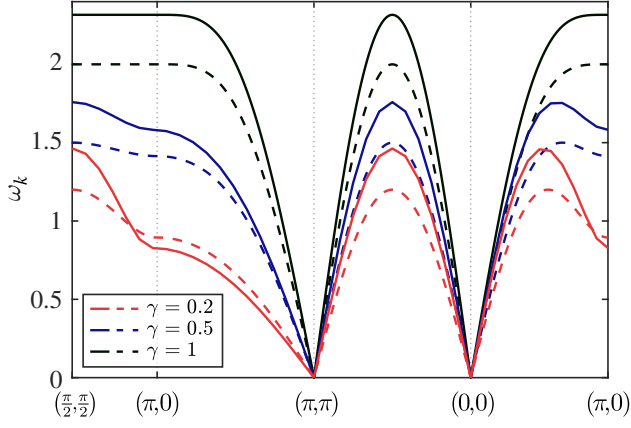


FIG. S2. **Self-consistent spin-wave spectra.** Renormalized spin-wave dispersion,  $\omega_k$ , calculated from Eq. (S20) (solid lines) and compared with the magnon dispersion of linear spin-wave theory (dashed lines) for  $\gamma = 0.2, 0.5$ , and 1.

### S3. SELF-CONSISTENT SPIN-WAVE THEORY

To gain further insight into the spin excitation spectra of the rectangular lattice with different  $\gamma$ , we also performed calculations of the one-magnon excitation branch expected within spin-wave theory. For an accurate analysis beyond the linear level, we follow the self-consistent method introduced by Oguchi [48] to compute the spin-wave spectrum at fourth order in the Holstein-Primakoff [47] operators  $a_i^\dagger$  and  $a_i$ , which are respectively bosonic creation and annihilation operators for a  $\Delta S = 1$  process on lattice site  $i$ . This level of treatment is equivalent to order  $1/S^2$ , or the Hartree-Fock diagrams.

Applying the Wick theorem to the four-operator terms requires the definition of the expectation values,

$$\begin{aligned} n &= \langle a_i^\dagger a_i \rangle, & t_\tau &= \langle a_i^\dagger a_{i+\tau} \rangle = \langle a_i a_{i+\tau}^\dagger \rangle, \\ \delta &= \langle a_i a_i \rangle = \langle a_i^\dagger a_i^\dagger \rangle, & \Delta_\tau &= \langle a_i a_{i+\tau} \rangle = \langle a_i^\dagger a_{i+\tau}^\dagger \rangle, \end{aligned}$$

where we restrict  $\tau \in \hat{x}, \hat{y}$  to nearest-neighbor sites only. These quantities are taken to be uniform for all sites of the rectangular lattice, although  $t_\tau$  and  $\Delta_\tau$  can differ with the direction of  $\tau$ . By treating these expectation values as mean fields, the quartic boson terms are decoupled to a quadratic form and the spin-wave dispersion relation is altered from the

conventional linear spin-wave form for an antiferromagnet,

$$\omega_k^0 = \sqrt{A_k^2 + B_k^2} \quad (\text{S19})$$

to the self-consistent form

$$\omega_k = \sqrt{(A_k + dA_k)^2 + (B_k + dB_k)^2}. \quad (\text{S20})$$

The mean fields can be computed from the ground state of the quadratic Hamiltonian in terms of the standard (hyperbolic Bogoliubov) coefficients

$$u_k = \sqrt{\frac{1}{2} \left( \frac{A_k}{\omega_k^0} + 1 \right)}, \quad v_k = \text{sgn}(B_k) \sqrt{\frac{1}{2} \left( \frac{A_k}{\omega_k^0} - 1 \right)},$$

as

$$\begin{aligned} n &= \frac{1}{N} \sum_k v_k^2, & t_\tau &= \frac{1}{N} \sum_k \cos(k \cdot \tau) v_k^2, \\ \delta &= \frac{1}{N} \sum_k u_k v_k, & \Delta_\tau &= \frac{1}{N} \sum_k \cos(k \cdot \tau) u_k v_k. \end{aligned}$$

Symmetry ensures that  $u_{k \pm Q} = u_k$  and  $v_{k \pm Q} = -v_k$ , as a result of which  $\delta = 0$ . Similarly, with  $\tau$  including only nearest-neighbor sites,  $t_\tau$  also vanishes. The renormalization terms in the self-consistent spin-wave dispersion [Eq. (S20)] then become

$$dA_k = \sum_\tau J_\tau dA_k^\tau \quad \text{and} \quad dB_k = \sum_\tau J_\tau dB_k^\tau \quad (\text{S21})$$

with

$$dA_k^\tau = 2(\Delta_\tau - n) \quad \text{and} \quad dB_k^\tau = 2(n - \Delta_\tau) \cos(k \cdot \tau). \quad (\text{S22})$$

The renormalization of the linear spin-wave energies can be codified in the factor  $Z_c(\mathbf{k}) = \omega_k / \omega_k^0$ . At  $\gamma = 1$ ,  $Z_c = 1.158$  becomes  $\mathbf{k}$ -independent, providing an excellent approximation to the correction  $Z_c = 1.18$  deduced from the nonlinear sigma model [46]. Figure S2 shows the spin-wave dispersions computed from Eq. (S20) for three different values of  $\gamma$ , which illustrate the qualitative extent both of the correction and of the  $\mathbf{k}$ -dependence at arbitrary  $\gamma$ . The dispersion relations for  $\gamma = 0.5$  and 1 in Fig. S2 are shown as the black lines in Figs. 2(c) and 2(d) of the main text.